5-2024

Microwave Imaging Technique for Breast Cancer Detection

Nure Alam Chowdhury
Florida Institute of Technology, nchowdhury2022@my.fit.edu

Microwave Imaging Technique for Breast Cancer Detection

by

Nure Alam Chowdhury

A thesis submitted to the College of Engineering and Science of
Florida Institute of Technology
in partial fulfillment of the requirements
for the degree of

Master of Science
in
Biomedical Engineering

Melbourne, Florida
May, 2024

We the undersigned committee hereby approve the attached thesis,
"Microwave Imaging Technique for Breast Cancer Detection"
by
Nure Alam Chowdhury

_____

Mehmet Kaya, Ph.D.
Associate Professor
Biomedical Engineering and Science
Major Advisor

_____

Linxia Gu, Ph.D.
Professor and Department Head
Biomedical Engineering and Science

_____

Kenia Pedrosa Nunes, Ph.D.
Associate Professor
Biomedical Engineering and Science

Abstract

Title: Microwave Imaging Technique for Breast Cancer Detection

Author: Nure Alam Chowdhury

Advisor: Mehmet Kaya, Ph.D.

Breast cancer is a global problem, and it is inevitable to detect cancerous cells at early stages. In recent years, microwave imaging technology has been widely applied in biomedical applications for its non-ionizing radiation. In this study, we design a microstrip patch antenna with an inverted T-type notch in the partial ground to detect tumor cells inside the human breast. The size of the current antenna is small enough (18 mm × 21 mm × 1.6 mm) to distribute around the breast phantom. The operating frequency has been observed from 6–14 GHz with a minimum return loss of −61.18 dB and the maximum gain of current proposed antenna is 5.8 dBi which is flexible with respect to the size of antenna. After the distribution of eight antennas around the breast phantom, the return loss curves have been observed in the presence and absence of tumor cells inside the breast phantom, and these observations show a sharp difference between the presence and absence of tumor cells. The simulated results show that this proposed antenna is suitable for early detection of cancerous cells inside the breast.

Table of Contents

List of Figures

List of Tables

Acknowledgement

The research hereby presented was possible with the guidance and continuous inspiration provided by my supervisor Dr. Mehmet Kaya and co-supervisor Dr. Linxia Gu. Nure Alam Chowdhury is grateful to Dr. Lulu Wang (Biomedical Device Innovation Center, Shenzhen Technology University, Shenzhen, 518118, China) for her proper guidance and suggestions to complete this reserch. Nure Alam Chowdhury is also thankful to Mr. S. M. Kayser Azam (Department of Electrical Engineering, University of Malaya, Malaysia) and Mr. Md. Shazzadul Islam (Electrical and Computer Engineering, Iowa State University, USA) for their support and discussions.

Dedication

Nure Alam Chowdhury would like to dedicate this research work to the freedom fighters of Bangladesh.

Chapter 1
Introduction

The final state of the irregular growth of the cell, which is also known as cancerous cell, inside the breast is considered as a breast tumor [1]. The time evolution of these inhomogeneous metastatic cancerous cells can spread to different sensitive parts of the body, viz., lungs, liver, and brain, etc. In 2008, a breast cancer test report stated that the number of breast cancer patients had increased by 20 percent and the death rate was almost 14 percent. In 2012, 1.7 million women were taking treatment for breast cancer [1]. So, this is a global problem, and it is inevitable to detect cancerous cells ormalignant tissue in specific areas of the body before further spread out to other parts of the body [2–4]. The early detection of breast cancer is vital for providing a suitable treatment corresponding to the status of breast cancer. If doctors can detect breast cancer before extreme situations, then the patients can receive proper treatment before further augmentation of cancer [4]. Different methods have been employed to detect breast cancer [4], viz., mammography, ultra-sound, positron emission tomography (PET), computed tomography (CT) scan, X-ray, Nuclear Magnetic Imaging Resonance (NMRI), and microwave imaging technigue (MIT), etc. But there are several limitations to employing these methods [4]. The mammography has a high sensitivity of 97% [5], a specificity of 64.5% [5], a positive predictive value of 89% [5], and a negative predictive value of 90.9% [5], a diagnostic accuracy of 89.3% [5] but this technique has several limitations, viz., ionizing radiations are used [6], the density of the breast affects the sensitivity and specificity [6], limited dynamic range, low-contrast, and grainy image due to the sensitivity drops with tissue [5], etc. Ultrasound is not suitable for bony structure image

even this method has a sensitivity of 80% [7] and a specificity of 88.4% [7]. Ultrasound provides a low-resolution image, and experienced operator is required during examination [6]. People also consider PET for screening of breast tumor. The sensitivity of PET is 68% for a tumor less than 2 cm [8] and 92% for a tumor of 2 cm to 5 cm [9], and the overall accuracy for detecting in situ carcinomas is low (sensitivity: 2-25%) [8]. PET has some disadvantages, viz., this method is an expensive method, uses ionized radiation [6], has limited resolution and slow imaging time [6], etc. CT scan is an effective method to early diagnosis of breast cancer due to its sensitivity (84.21%), specificity (99.3%), and accuracy (98.68%) but still this method has limitation, i.e., successive CT scanning of radiosensitive organs like breast can cause long term effects [10]. When experts can observe initial symptoms associated with breast cancer in the patients, they suggest applying an x-ray to the breast to collect an X-ray image for further observation and determination of the breast cancer [11]. Sometimes, fluid-fill lymph is to be cancerous and is considered less dangerous than solid lymph. If there is a signature of fluid fill or lymph of solid, the breast is considered for an ultra-sound checkup for further confirmation of breast cancer fill [7]. On the other hand, some specific cells from a particular regime associated with breast cancer can be removed by breast biopsy [12]. The X-rays can produce ionizing radiation, and we know that successive application of the ionizing radiation, hence, can change the internal structure of the breast tissues [1]. NMRI and ultra-sound, which are free from the ionizing radiation, are effective ways for observing the cancerous cells inside the breast but these methods are very expensive. NMRI and ultra-sound instruments are not available all over the world. On the other hand, the physical mechanism of the NMRI is related to nuclear science. Some patients

feel fear when they are diagnosed by NMRI. So, it is essential to find another way for early detection of cancerous cells inside thewomen's breast. In that case, the best option is MIT for early detection of different cancerous cells inside body [2, 4]. On the other hand, for biomedical applications, the most suitable range of frequency associated with antenna is ultra-wide band (UWB) [2, 4]. Several research groups worldwide have been studying the use of microwaves for medical applications, especially for breast cancer screening [13, 14]. Microwaves are high-frequency, non-ionizing electromagnetic radiation used in our daily devices like mobile phones [15]. Low-power microwave technology is currently easily accessible, low cost, and poses no health risk, etc. Complex permittivity is one of the material properties that dictates its response to electromagnetic waves [2, 4]. It measures how molecules dynamically deform subject to the alternating applied electromagnetic fields. Different tissues, forming the breast internal structures, present complex permittivity [15]. If the contrast between the permittivity of various materials is high enough, this variation of permittivity leads the incident electromagnetic wave to reflect at the boundary. The dielectric constant of a matter describes the dielectric characteristics of the material [16-18]. The value of the dielectric constant associated with specific material can represent the ability to absorb energy from an electric field. The smaller the dielectric constant value, the less energy is absorbed from an electric field. Antenna has been considered one of the most important technical constructions for transmitting and receiving electromagnetic waves in free space and is applicable to wireless communications [16], radar communications [15], and biomedical applications [1], etc. The size and shape of the antenna play an important role in the physical outputs associated with antenna. Another important parameter for antenna's

outcomes is the frequency at which it will be operated [16, 17]. The size and shape of the antenna are also related to the operating frequency [16, 17]. The Federal Communication Commission (FCC) assigned different names corresponding to different frequency ranges, and the FCC declared 3.1 to 10.6GHz as ultra-UWB regime [1, 2]. To obtain physical and applicable outcomes from an antenna associated with ultra-wideband frequency range, people consider different geometry (e.g., partial ground [3], coplanar, slots [16], strips [16], and notch [17], etc.) for designing the antenna.

1.1 Literature Review

Currently, researchers consider different antennas as an imaging tool for the early detection of breast cancer [18-23]. In [12], a planarmonopole antenna has been designed for an operating frequency 7–14GHz, and the associated return loss, gain, and efficiency of the proposed antenna have been observed for a specific orientation of a single antenna around the breast phantom. In [18], the author designed a microstrip patch antenna for observing different physical properties (viz., electric field, magnetic field, and current density, etc.) in the presence and absence of a tumor inside the breast. The number of antennas around the breast phantomplays an important role in collecting large-scale data to precisely determine the size and location of a tumor. Comprehensive information about the different breast components can be achieved by considering more antennas around the breast phantom. On the other hand, the tumor can exist in any arbitrary location inside the breast. In [24], a square patch antenna has been considered to observe the specific absorption rate (SAR) of a tumor inside the breast phantom in the presence and absence of a tumor. In [25], the authors considered a single antenna 20 mm away from the breast phantom and observed a tumor in

a specific location inside the breast phantomby studying the SARvalue. It is important to study the existence of tumorswith different sizes and locations inside the phantom in the presence of multiple antennas around the breast phantom.

1.2 Objectives

In this work, we will design a microstrip patch antenna with an inverted T-type notch in the partial ground and will distribute 8 antennas around the breast phantom for comprehensive data collection of different mediums of breast phantom.We will also consider different size of the tumor in a specific location as well as an arbitrary location with a specific size of tumor inside the breast phantom for early detection of breast tumor.

Chapter 2
Antenna Design

The perfect design of an antenna can precisely predict the physically applicable outcomes. It is very important to consider available material to construct a new antenna. FR4 substrate is a commonly used low-cost substrate that has relatively high dielectric loss and is considered lossy compared to other high-performance substrates such as RT/Duroid. However, FR4 substrate can still be useful in the frequency range of 6 to 14GHz because its loss tangent is relatively low in this frequency range, which means that the dielectric losses are not as significant as they would be at higher frequencies. Additionally, the high dielectric constant of FR4 substrate allows for compact antenna designs, which can be advantageous in certain applications where size and weight are critical factors. Therefore, the authors may have chosen to use FR4 substrate in this frequency range to take advantage of its low cost, compact size, and relatively low dielectric losses. Several authors considered FR4 substrate to design antenna for different ranges of operating frequency [26-30]. In [26], the authors considered FR4 substrate to design an antenna which can be operated in a frequency range of 2.5 to 29.0GHz. In [27], a Koch-fractal antenna has been designed on FR4 substrate and the proposed antenna can operate in the frequency range from 2 to 30GHz. In [28], a FR4 substrate has been considered to design star-triangular fractal monopole antenna which can operate in a frequency range of 1 to 30GHz. The substrate for the current antenna has been considered FR4 lossy material (tangent loss is 0.02) which has a relative permittivity of 4.4. We used ANSYS HFSS software for designing the antenna corresponding microstrip feedline of 50-ohm impedance power source and for validation of antenna results, we also

used CST STUDIO SUITE to design single antenna. The basic governing equations for the microstrip patch width and length can be expressed as [31-35].

$$\text{Patch width (PW)} = \frac{c}{2f_0\sqrt{\frac{\varepsilon_r+1}{2}}}, \quad (1)$$

$$\text{Patch length (PL)} = \frac{c}{2f_0\sqrt{\varepsilon_{eff}}} - 0.824h\left[\frac{(\varepsilon_{eff}+0.3)\left(\frac{PW}{h}+0.264\right)}{(\varepsilon_{eff}-0.258)\left(\frac{PW}{h}+0.8\right)}\right], \quad (2)$$

where c is the light speed in the vacuum, f_0 represents the operating frequency, ε_r express the relative permittivity of the substrate, h is the height of the substrate, PW is the width of the patch, and ε_{eff} is the effective dielectric constant which can be written as

$$\varepsilon_{eff} = \frac{\varepsilon_r+1}{2} + \frac{\varepsilon_r-1}{2\sqrt{1+12\left(\frac{h}{PW}\right)}}. \quad (3)$$

The microstrip feed line characteristic impedance can be calculated by employing this equation [1]

$$Z_0 = \frac{120\pi}{\sqrt{\varepsilon_{eff}}\left[\frac{FW}{h}+1.393+0.667\ln\left(\frac{FW}{h}+1.444\right)\right]}, \quad (4)$$

where FW is the width of the microstrip feed line. Ground plane width and length are calculated with the following formula, respectively [36-38]:

$$\text{Ground plane width (GW)} = PW + 6h, \quad (5)$$

$$\text{Ground plane length (GL)} = PL + 6h. \quad (6)$$

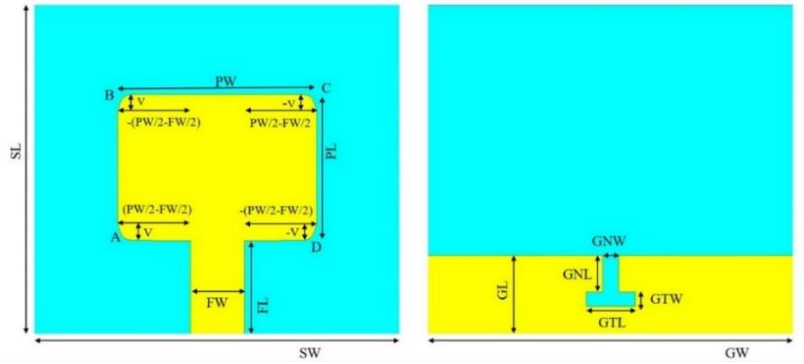

Figure 2.1: Final design of the antenna.

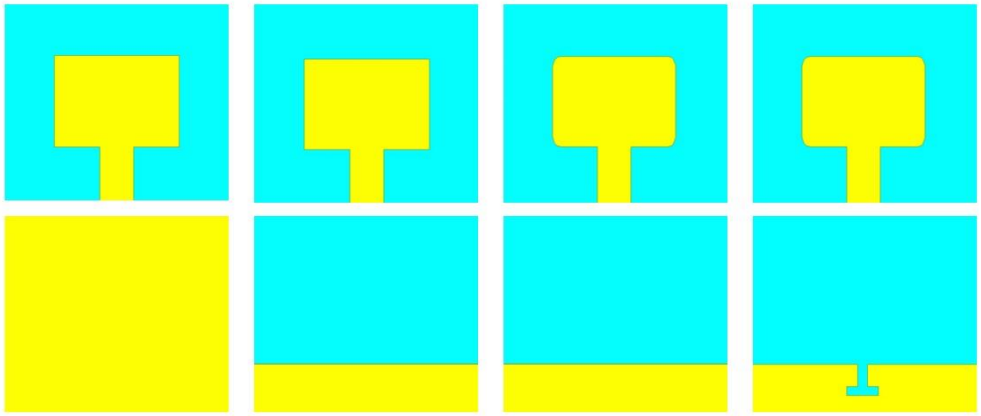

Figure 2.2: Four successive iteration for antenna design.

The final design of the proposed antenna can be seen in Fig. 2.1. For designing the final proposed antenna, we employ four successive iterations to find physically applicable outcomes. In the zeroth iteration [please see Fig. 2.2a, upper-panel (microstrip patch) and lower-panel (full ground)], we design a simple microstrip patch and a full ground by applying Eqs. (1)–(6). Then, in the first iteration (see Fig. 2.2b, lower panel), we make our full ground to a partial ground and optimize the length of the partial ground (GL) to find the minimum

return loss, and the better optimized GL is observed at 4.3mm (the figure is not included). In the second iteration, we employ four exponential equations in each corner of the microstrip patch and observe a rigorous increment of the frequency bandwidth (please see Fig. 2.2c, upper panel). The equations, which have been employed in the patch at each corner, are represented in Table 2.1.

Table 2.1: Patch corner equations.

Corner	Equation	Start u	End u	Start v	End v
A	$v * \exp(-rate * u)$	0	PW/2-FW/2	V	0
B	$v * \exp(rate * u)$	0	-(PW/2-FW/2)	V	0
C	$v * \exp(-rate * u)$	0	PW/2-FW/2	-V	0
D	$v * \exp(rate * u)$	0	-(PW/2-FW/2)	-V	0

In the third iteration, we have included an inverted T-type notch in the partial ground directly opposite to the microstrip feed line (please see Fig. 2.2d, lower panel) without any further changing over the patch. The T-notch has been chosen because it provides a wide bandwidth and deep frequency rejection. The slotted antenna achieves larger gain and efficiency by exciting a resonant mode in the slot and coupling it to the main radiator. The slot can improve the antenna performance by reducing surface wave losses and enhancing radiation efficiency, but the design must carefully balance the slot size and position to avoid degrading the performance. In this case, the performance improvement was achieved by optimizing the dimensions and position of the slot to enhance radiation efficiency and reduce losses. This inverted T-type notch significantly minimizes the return loss of the current design of antenna

and establishes a proper impedance matching between the external power source and the antenna. The designing parameters associated with the new antenna design are presented in Table 2.2.

Table 2.2: Different parameters related to antenna.

Antenna parameters	Dimensions (mm)	Antenna parameters	Dimensions (mm)
Length of substrate (SL)	18	Ground width (GW)	21
Width of substrate (SW)	21	GNL	02
Thickness of substrate (h)	1.6	GNW	0.9
Length of patch (PL)	08	GTL	2.8
Width of patch (PW)	11.4	GTW	0.8
Length of feed line (FL)	5.1	V	0.9
Width of feed line (FW)	3.1	rate	5000
Ground length (GL)	4.3		

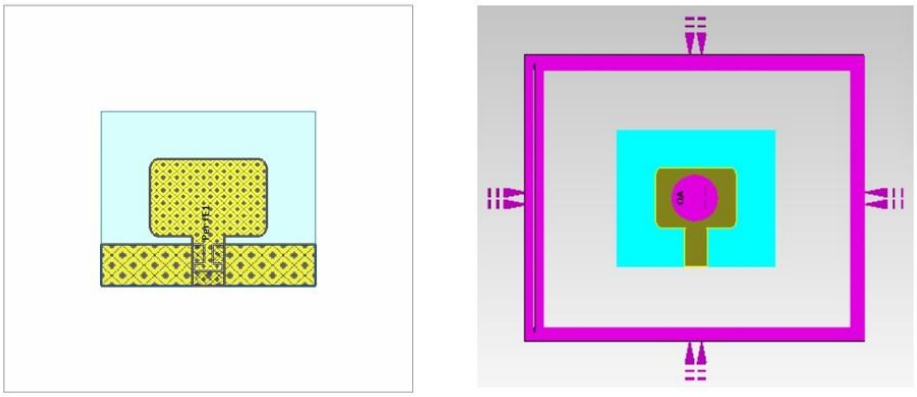

Figure 2.3: Simulation setup of ANSYS HFSS (left panel) and CST STUDIO SUITE (right panel).

The left panel of Fig. 2.3 represents the simulation setup of ANSYS HFSS. The box, which encloses the antenna, is the radiation box, and air is considered inside the radiation box. On

the other hand, the right panel of Fig. 2.3 represents the simulation setup of CST STUDIO SUITE.

The proper design of an antenna for MWI is a great challenge [16, 17]. Especially, when it comes near to the human body. Because the human body acts as a dielectric lossy material and the discontinuity of different dielectric properties of the human body, the radiating power of an antenna can be degraded or absorbed [16, 17]. While designing antennas that are working near to the human body for different applications, especially for MWI, these drawbacks must be considered. Microstrips are also susceptible to electromagnetic interference (EMI) from nearby electronic devices, including 5G phones, Wi-Fi routers, and other high-frequency sources, etc. This interference can cause signal degradation, increase noise levels, and reduce performance of the microstrip circuit, etc. To mitigate these interferences, proper shielding techniques, grounding, and careful layout design should be implemented.

Chapter 3
Breast Phantom Dielectric Properties

The structure of a real breast is very complex which has different components, viz., skin, fat, fibro-gland, muscle, artery, blood, and water, etc. So, it is very difficult to address all the components and their dynamic properties in a single framework to run a simulation. In this perspective, people consider a simple static structure which has three fundamental components, viz., breast skin, breast fat, and breast fibro-gland [39], etc. The density of different parts of the breast phantom remains constant over the frequency range at which the antenna is going to work but other physical properties like relative permittivity, conductivity, and the loss tangent of the different parts of the breast phantom are going to change according to the operating frequency [40-43]. Table 3.1 shows the physical properties of the breast phantom at a specific frequency of 8GHz [40-43].

Table 3.1: Physical properties of the different components of the breast phantom.

Breast components	Density	Relative permittivity	Conductivity [S/m]	$\tan\delta$
Breast skin	1010	33.14	5.82	0.394
Breast fat	928	4.14	0.6	0.325
Breast Fibro-gland	1035	48.42	8.96	0.415
Breast tumor	1077	55.42	10	0.56

Chapter 4
Modeling of a Human Breast Phantom

A half spherical shaped breast phantom with three different layers (viz., breast skin, breast fat, and breast fibro-gland, etc.) can be seen in Fig. 4.1. The outer layer of the breast is the breast skin. After this layer, there is a fat layer which is represented by the yellow color in Fig. 4.1, and finally a layer of fibro-gland is just living center/middle of the half spherical shaped breast phantom [1].

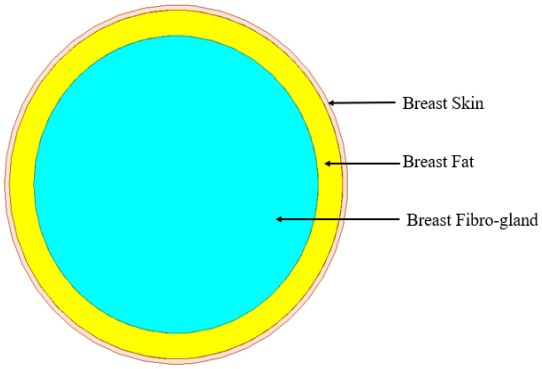

Figure 4.1: **:** Cross-sectional view of different components of the breast phantom.

The radius as well as the thickness of the different parts of the breast phantom are different [1]. Here we present the thickness of different layers of the breast phantom in Table 4.1.

Table 4.1: The thickness of the different parts of the breast phantom.

Breast phantom components	Dimensions (mm)
Breast skin	2
Breast fat	10
Breast fibro-gland	68
Breast tumor	10

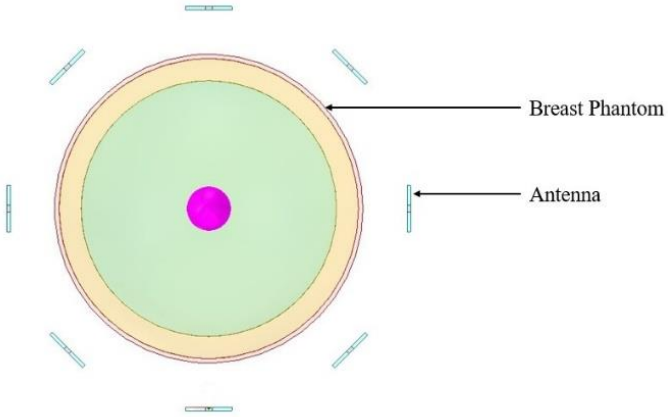

Figure 4.2: The presence of breast tumor inside the breast phantom and the distribution of 8 antennas around the breast phantom (ANSYS HFSS).

The time evolution of cancerous cells transforms into tumors. So, these tumors are living inside the breast phantom. In Fig. 4.2, a tumor can be seen in the middle of the half spherical shaped breast phantom. There are 8 antennas array around the phantom. The antenna array is 20 mm far away from the skin/outer layer of the half spherical shaped breast phantom for making a good impedance matching. The center of each antenna makes an angle 45 degrees (360/8=45 degrees) with the center of the next antenna corresponding to the center of the breast phantom in the same plane.

Chapter 5
Results and Discussion

5.1 Single Antenna Performance Analysis

The return loss curve describes the amount of power of an antenna is going to return in the backward direction when the antenna operates. If the return loss is minimum for an antenna that means the antenna can transmit maximum power. For designing the antenna, we considered four successive iterations to find better physical outcomes. Here we would like to discuss the return loss associated with a single antenna.

The variation of return losswith frequency for different iterations of a single antenna can be seen in Fig. 5.1a. It can be seen from this figure that after completing the first iteration, the return loss touches −25.60 dB from −5.22 dB at 8GHz. In the second iteration, the return loss decreases to −38.59 dB from−25.60 dB, and theminimumreturn loss is observed at−61.18 dB corresponding to the frequency of 8GHz after completing the third iteration (please see Fig. 2.2 for the detail of designing iterations of current proposed antenna). It is interesting that our proposed antenna can operate a frequency range from6 to 14GHz and theminimumreturn loss is observed at 8GHz. Fig. 5.1b expresses the comparison of return loss curve of ASYSHFSS and CST STUDIO SUITE design. It can be seen fromFig. 6b that (i) the operating frequency has been observed almost same from 6–14GHz for both ASYS HFSS and CST STUDIO SUITE antenna designs; (ii) both antenna designs provide a resonance at 8GHz.

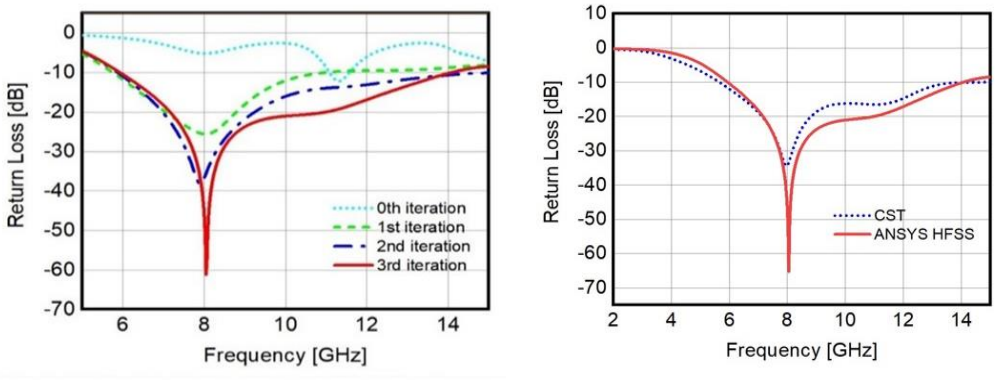

Figure 5.1: (a) Return loss for four successive steps (ANSYS HFSS), and (b) the comparison of return loss curves.

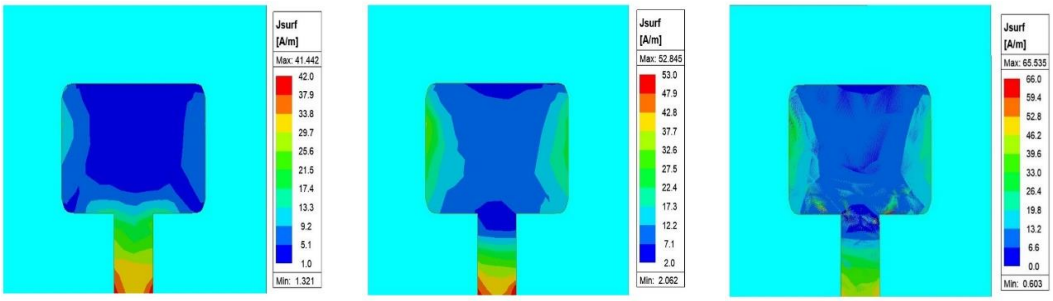

Figure 5.2: Current distribution over the patch at (a) 6 GHz; (b) 8 GHz; and (c) 12 GHz (ANSYS HFSS).

The distribution of the surface current above the patch can be observed in Fig. 5.2 and it can be seen from this figure that (a) most of the surface current is distributed over the microstrip feedline and the edges of the microstrip patch; (b) the maximum value of the surface current density are 41.442 A/m, 52.845 A/m, and 65.535 A/m corresponding to the frequency of 6 GHz, 8 GHz, and 12 GHz; (b) the minimum surface current is observed in the center and near to the center of the patch; (c) the maximum surface current density increases with the

increase in the value of frequency; (d) physically, due to skin effect, with increasing the frequency, most of the charges are living above the surface of the patch and microstrip feedline.

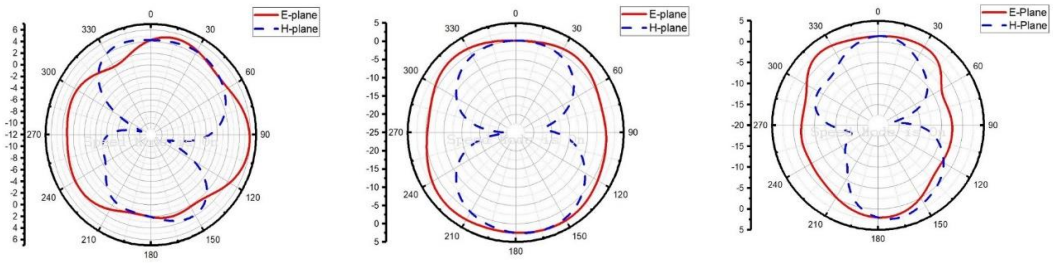

(a) 6.0 GHz (b) 8.0 GHz (c) 10 GHz

Figure 5.3: 2D gain plots of the suggested antenna at a frequency of (a) 6.0 GHz, (b) 8.0 GHz, (c) 10 GHz (ANSYS HFSS).

The radiation pattern, which describes the direction of the propagation of the antenna radiation, is very important to apply in different physical situations. The radiation pattern of proposed antenna for different frequencies can be observed in Fig. 5.3. It is clear from this figure that (a) for frequency 6 GHz, the radiation pattern in the E-plane (i.e., $\phi = 0$) is almost omnidirectional; (b) a pure omnidirectional radiation pattern in the E-plane (i.e., $\phi = 0$) can be observed at frequency 8 GHz; (c) the radiation pattern in the E-plane (i.e., $\phi = 0$) seems to be distorted from omnidirectional at frequency 10 GHz. On the other hand, in the H-plane (i.e., $\phi = 90$), the radiation pattern looks bidirectional for the frequencies 6.0 GHz, 8.0 GHz, and 10 GHz, etc.

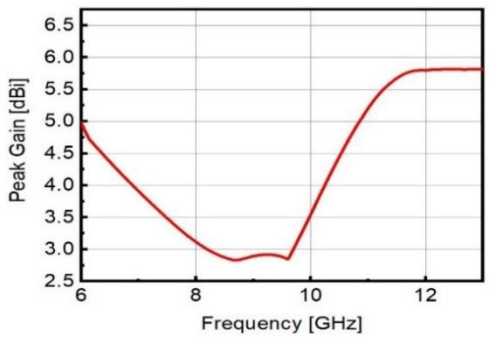

Figure 5.4: Peak gain vs. frequency curve (ANSYS HFSS).

The relation between the peak gain with frequency can be observed from Fig. 5.4. Initially, the peak gain is 4.97dBi at 6 GHz then it slowly decreases to 2.83 dBi at 8.7 GHz and remains almost constant (below 3dBi) up to around 9.6 GHz and again the peak gain linearly increases to 5.8 dBi at 11.9 GHz. Finally, the peak gain remains almost constant from 11.9 GHz to 14 GHz, and in this frequency regime, the peak gain is around 5.7 dBi to 5.8 dBi. So, the maximum gain is observed at 5.8 dBi for the suggested antenna within the frequency band 6 GHz to 14 GHz.

5.2 Deep-Seated Breast Tumor Detection

Initially, we consider a spherical shaped tumor with a radius of 5 mm living inside the half spherical shaped breast phantom, and in that case, each antenna element maintains equal distance from the outer surface of the breast phantom and even from the center of the 5 mm tumor. Each antenna is 90 mm far away from the center of the tumor (see Fig. 5.5).

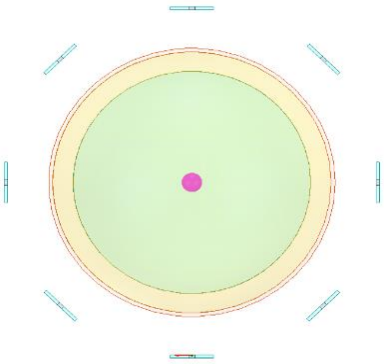

Figure 5.5: Deep-seated tumor with 5 mm radius.

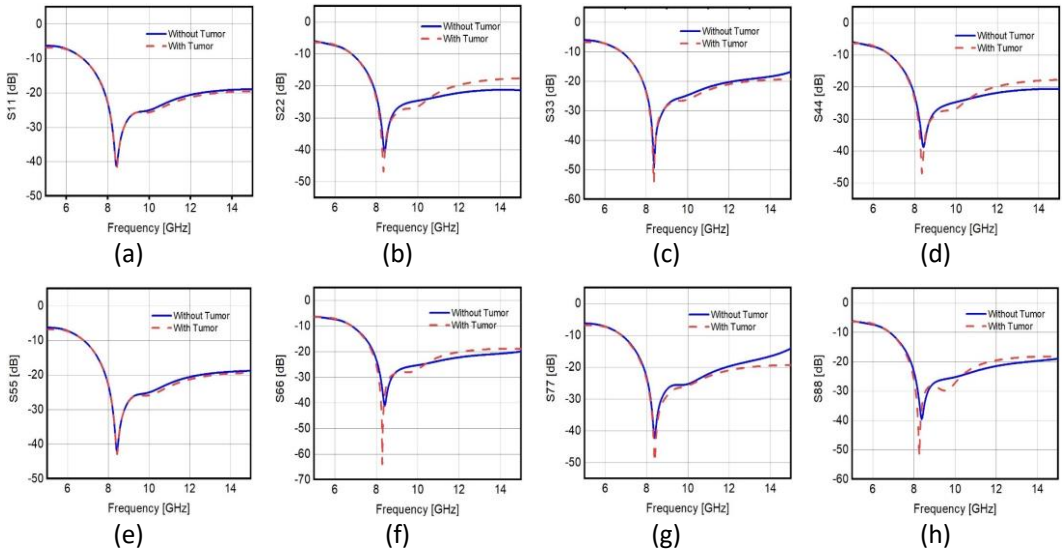

Figure 5.6: Return loss in the presence of a 5 mm tumor.

The return loss curves corresponding to a breast phantom without tumor and with a tumor, which exists in the deep-seated position of the breast phantom, can determine the presence or absence of the deep-seated tumor inside the breast phantom. Each panel of Fig. 5.6 shows both return loss curves corresponding to the existence of tumor (dashed red curves) and

without tumor (solid blue curves). It is clear from this figure that there is a sharp difference between each of the dashed red curves associated with the presence of a tumor and corresponding the solid blue curves associated with the absence of a tumor. This happens due to the dielectric properties of the existing deep-seated tumor inside the breast phantom. If there is no deep-seated tumor inside the breast phantom, then both solid and dotted curves from each panel of Fig. 5.6 will coincide with each other.

Now, we consider 10 mm radius of a spherical tumor in the same location to run a new simulation and would like to observe the ability of 8 antennas around the breast phantom to detect a tumor with a radius of 10 mm in the deep location of breast phantom (see Fig. 5.7).

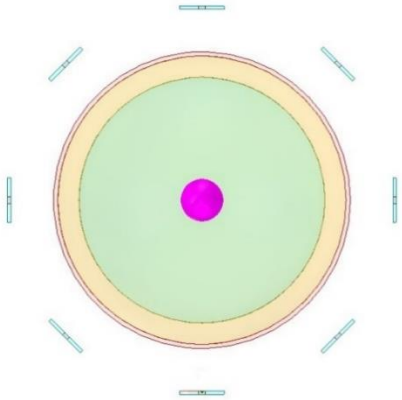

Figure 5.7: Deep-seated tumor with 10 mm radius.

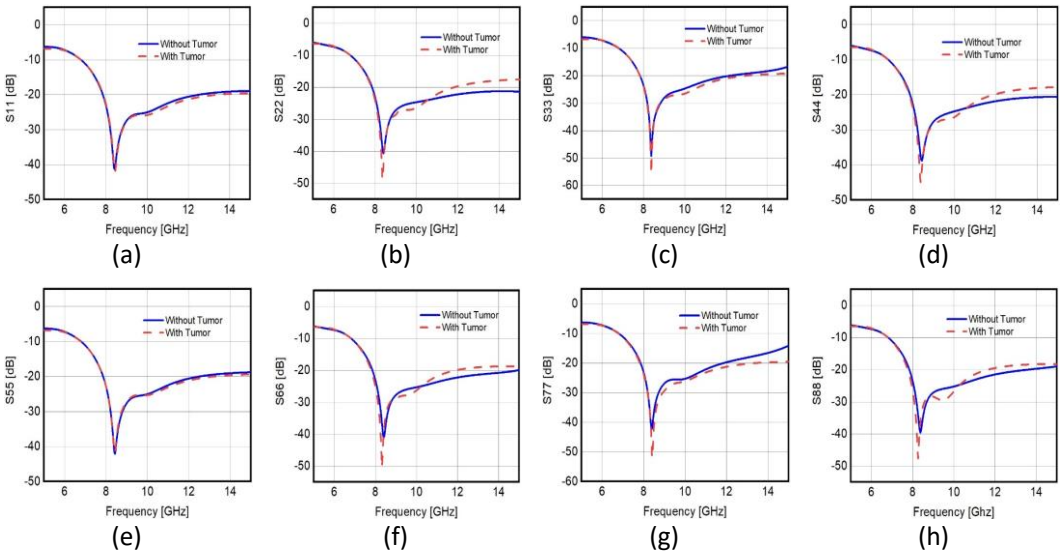

Figure 5.8: Return loss in the presence of a 10 mm tumor.

The return loss curves correspond to the presence of a 10 mm deep-seated tumor (dashed red curves), and the absence of the tumor (solid blue curve) again provide a sharp difference as well as tumor existence (see Fig. 5.8).

Now, we again consider a 15 mm deep-seated tumor inside the breast phantom (see Fig. 5.9), and Fig. 5.10 represents the return loss curves corresponding to existence and absence of tumor.

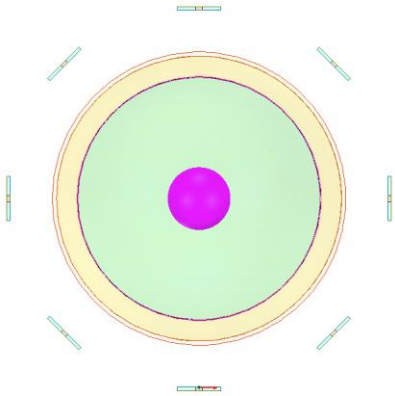

Figure 5.9: Deep-seated tumor with 15 mm radius.

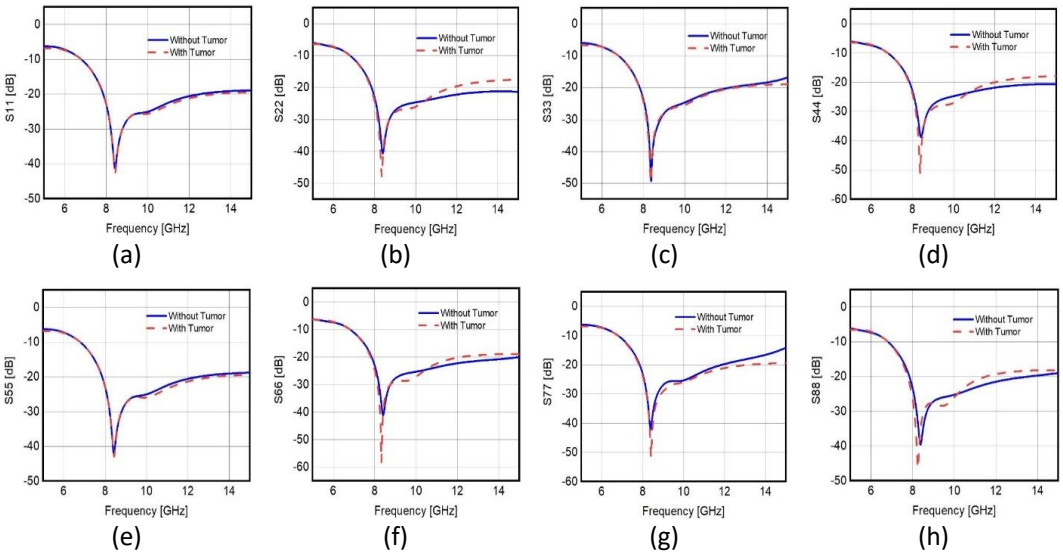

Figure 5.10: Return loss in the presence of a 15 mm tumor.

We can see from each panel of return loss curves that the dashed red curve corresponding to the existence of tumor inside the phantom and the solid blue curve corresponding to the absence of a tumor does not coincide with each other for each point of frequency. So, our suggested antenna can detect a deep-seated tumor with a radius of 5 mm, 10 mm, and 15 mm, etc.

Now, we are determining the numerical values of return loss for both the presence and absence of the tumor, and their differences for a 5 mm, 10 mm, and 15 mm radius of deep-seated tumors. The difference between the return loss values ($|\Delta S|$) of a breast phantom with and without a spherical tumor can be calculated as $|\Delta S| = \left|S_{ij(\text{without tumor})} \sim S_{ij(\text{with tumor})}\right|$, where and $i = j$ and $i, j = 1, 2, 3 \ldots$).

Table 5.1: The $|\Delta S|$ value for different size of deep-seated tumor for 8 GHz.

Reflection coefficient	Breast phantom without tumor	Breast phantom with a 5mm tumor ($|\Delta S|$)	Breast phantom with a 10 mm tumor ($|\Delta S|$)	Breast phantom with a 15 mm tumor ($|\Delta S|$)
$|S_{11}|$	-23.28	-23.03 (0.25)	-23.07 (0.21)	-22.90 (0.38)
$|S_{22}|$	-23.39	-24.35 (0.96)	-24.67 (1.28)	-24.38 (0.99)
$|S_{33}|$	-23.83	-24.38 (0.55)	-24.67 (0.84)	-24.25 (0.42)
$|S_{44}|$	-23.11	-24.21 (1.10)	-24.17 (1.06)	-24.31 (1.10)
$|S_{55}|$	-23.16	-22.93 (0.23)	-23.03 (0.13)	-23.23 (0.07)
$|S_{66}|$	-23.34	-25.51 (2.17)	-25.14 (1.80)	-25.40 (2.06)
$|S_{77}|$	-23.39	-24.18 (0.79)	-24.12 (0.73)	-24.01 (0.62)
$|S_{88}|$	-23.78	-26.74 (2.96)	-27.24 (3.46)	-26.86 (3.08)

Table 5.1 represents the detailed picture of numerical values of three different simulations (i.e., 5 mm, 10 mm, and 15 mm radius deep-seated tumor inside breast phantom and breast phantom without tumor). From this Table 5, for 5 mm deep-seated tumor, the lowest and highest values of ΔS are 0.23 dB and 2.96 dB, respectively, and for 10mm deep-seated tumor, the lowest and highest values of ΔS are 0.13 dB and 3.46 dB, respectively. Similarly, for a 15 mm deep-seated tumor, the lowest and highest values of ΔS are 0.07 dB and 3.08 dB, respectively. So, the current proposed antenna array can determine a tumor with different sizes within the half-spherical shaped breast phantom.

5.3 Superficially Located Breast Tumor Detection

Here we would like to discuss that the current antenna array is able to detect the existence of a spherical tumor with a 2 mm radius in different superficial locations inside the breast phantom. For this purpose, we change the tumor location from deep-seated position to different arbitrary positions. Different position of a spherical breast tumor with 2 mm radius can be seen in each panel

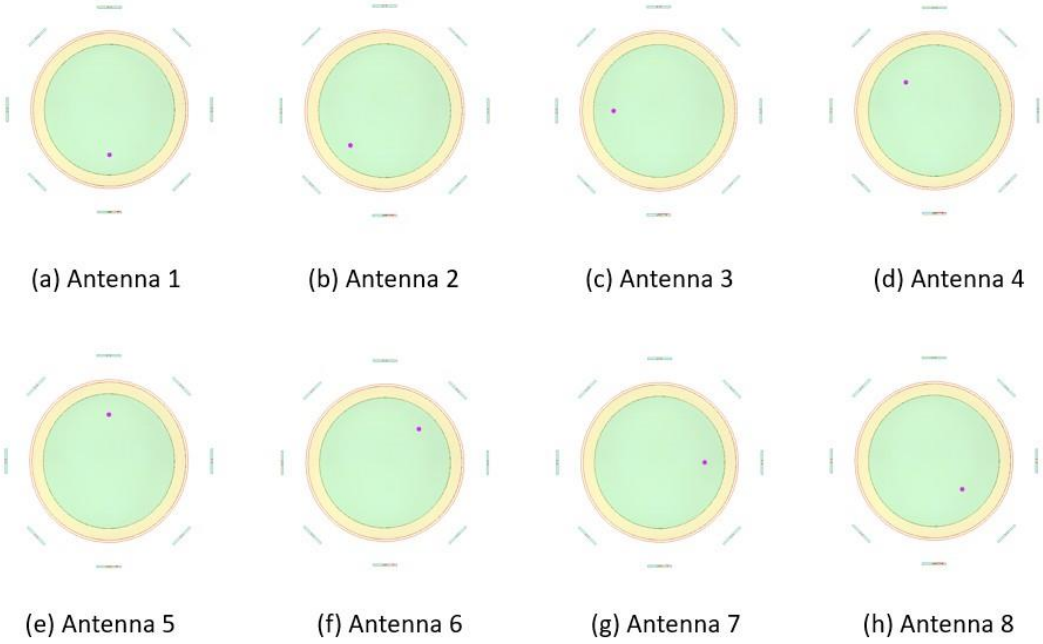

Figure 5.11: Different positions of a 3 mm tumor.

of Fig. 5.11. Each panel of Fig. 5.11 represents an arbitrary position of a 2 mm radius tumor; for example, Fig. 5.11a, a tumor with 2 mm radius exists near to antenna 1. Similarly, Fig. 5.11b and Fig. 5.11c, a tumor is present near antenna 2 and antenna 3, etc. Table 5.2 represents the ΔS values for different arbitrary positions of a 2 mm tumor inside the breast.

Table 5.2: ΔS values for different arbitrary positions of a 2 mm tumor.

Reflection Coefficients Difference (ΔS)	Antenna 1 (dB)	Antenna 2 (dB)	Antenna 3 (dB)	Antenna 4 (dB)	Antenna 5 (dB)	Antenna 6 (dB)	Antenna 7 (dB)	Antenna 8 (dB)
$\lvert\Delta S_{11}\rvert$	1.30	0.38	1.24	1.11	1.12	2.96	3.21	2.45
$\lvert\Delta S_{22}\rvert$	2.61	0.61	3.18	3.11	2.49	2.72	3.03	2.79
$\lvert\Delta S_{33}\rvert$	2.38	0.42	2.19	2.12	2.21	3.57	3.32	3.13
$\lvert\Delta S_{44}\rvert$	2.70	0.16	3.08	3.05	2.84	2.98	2.61	2.79
$\lvert\Delta S_{55}\rvert$	1.22	0.47	1.52	1.47	1.17	3.20	2.91	2.68
$\lvert\Delta S_{66}\rvert$	4.37	1.37	3.92	3.97	4.69	4.49	4.49	4.20
$\lvert\Delta S_{77}\rvert$	2.22	0.35	1.96	2.48	2.23	1.80	2.37	2.09
$\lvert\Delta S_{88}\rvert$	5.18	2.30	5.70	5.69	5.84	4.87	5.33	4.99

Similarly, we can consider the 5 mm radius of a spherical tumor in different arbitrary locations inside of the breast phantom (see Fig. 5.12). Table 5.3 represents the ΔS values for different arbitrary positions of a 5 mm tumor.

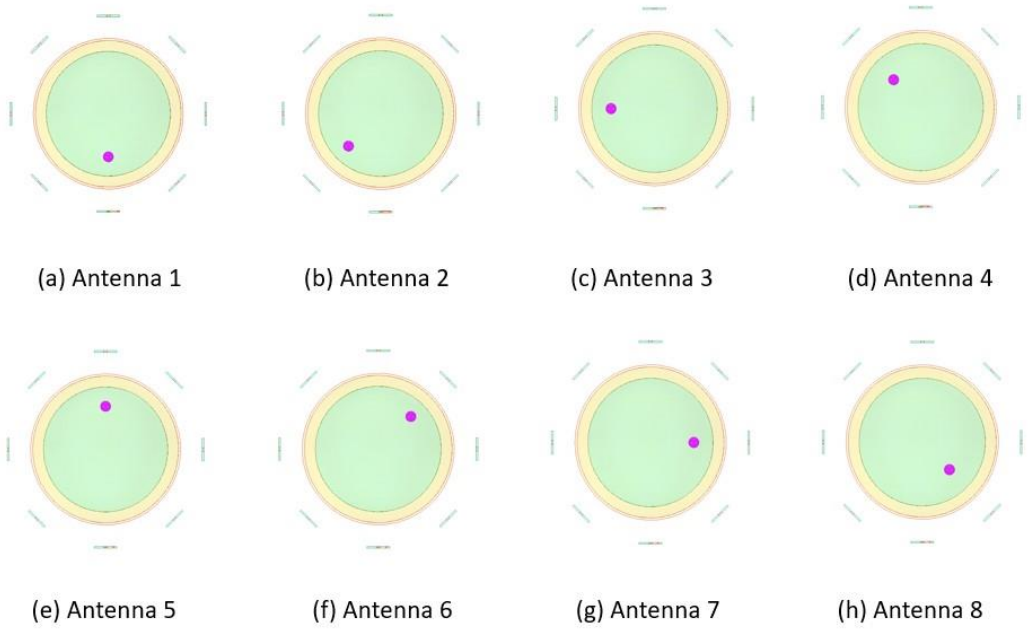

Figure 5.12: Different positions of a 5 mm tumor.

Table 5.3: ΔS values for different arbitrary positions of a 5 mm tumor.

Reflection Coefficients Difference (ΔS)	Antenna 1 (dB)	Antenna 2 (dB)	Antenna 3 (dB)	Antenna 4 (dB)	Antenna 5 (dB)	Antenna 6 (dB)	Antenna 7 (dB)	Antenna 8 (dB)
$\lvert\Delta S_{11}\rvert$	0.98	0.90	1.07	1.22	1.01	2.92	2.58	3.11
$\lvert\Delta S_{22}\rvert$	2.67	0.32	2.71	2.65	2.51	2.71	2.45	2.80
$\lvert\Delta S_{33}\rvert$	2.23	0.42	2.37	2.23	2.20	3.35	2.99	3.58
$\lvert\Delta S_{44}\rvert$	2.81	0.19	3.00	3.08	2.78	2.34	2.61	2.39
$\lvert\Delta S_{55}\rvert$	1.26	0.50	1.32	1.44	1.40	3.51	3.61	2.69
$\lvert\Delta S_{66}\rvert$	2.88	1.27	3.92	4.68	3.92	4.44	4.15	4.12

$\lvert\Delta S_{77}\rvert$	2.08	0.41	2.36	2.40	2.45	1.91	2.10	1.92
$\lvert\Delta S_{88}\rvert$	5.55	2.26	5.66	6.25	4.80	4.84	5.07	4.64

Again, a spherical size tumor with a 10 mm radius has been considered in different arbitrary locations inside of the breast phantom (see Fig. 5.13). Table 5.4 represents the ΔS values for different arbitrary positions of a 10 mm tumor.

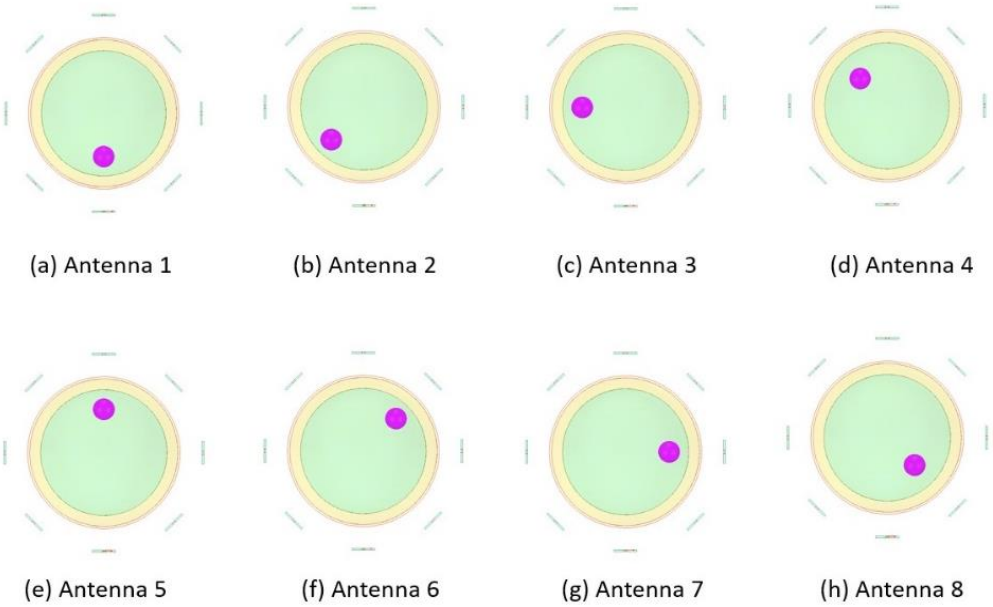

Figure 5.13: Different positions of a 10 mm tumor.

Table 5.4: ΔS values for different arbitrary positions of a 10 mm tumor.

Reflection Coefficients Difference	Antenna 1 (dB)	Antenna 2 (dB)	Antenna 3 (dB)	Antenna 4 (dB)	Antenna 5 (dB)	Antenna 6 (dB)	Antenna 7 (dB)	Antenna 8 (dB)

(ΔS)								
$\lvert\Delta S_{11}\rvert$	0.59	0.98	0.53	1.00	0.18	1.53	0.90	2.93
$\lvert\Delta S_{22}\rvert$	2.03	1.18	1.17	0.97	2.00	0.30	1.51	0.54
$\lvert\Delta S_{33}\rvert$	0.32	0.98	0.46	0.87	0.13	1.98	0.55	3.24
$\lvert\Delta S_{44}\rvert$	0.34	0.95	0.52	1.23	0.24	2.16	0.75	3.05
$\lvert\Delta S_{55}\rvert$	0.57	0.82	1.25	1.05	0.17	1.91	0.97	3.35
$\lvert\Delta S_{66}\rvert$	1.2	0.87	1.56	0.87	1.26	1.98	0.38	2.84
$\lvert\Delta S_{77}\rvert$	0.98	1.12	1.5	0.99	1.03	1.98	0.7	2.41
$\lvert\Delta S_{88}\rvert$	1.09	1.29	1.76	1.01	1.42	2.03	0.86	2.24

Table 5.2, 5.3, and 5.4 represent the difference between the return losses in the absence and presence of a tumor with different radius in an arbitrary position associated with 8 simulations, and each ΔS has a significant value to clearly differentiate the cancerous cells inside the breast phantom. So, the suggested antenna array is not only suitable for the detection of the deep-seated tumor but also suitable for a superficially located tumor inside the breast phantom.

Chapter 6
Comparison of Current Research Outcomes with the Existing Literature

Now, we are looking at a comparison between the current proposed antenna with others existing antennas. In that case, we consider the substrate, size, operating frequency, return loss, and maximum gain, etc.

Table 6.1: Comparison of current outcomes with published works.

References	Substrate	Dimension (mm^2)	Operating frequency range (GHz)	Minimum return loss	Maximum gain	Cancer detection ability
[18]	FR4	65×89	2.45 GHz	Not given	not given	able to determine
[19]	FR4	24×34	2.4 GHz-4.7 GHz	-33 dB	not given	able to determine
[20]	Rogers 5880	40×48	2.45 GHz	-31 dB	not given	able to determine
[21]	Felt	60×60	3.1 GHz-10.6 GHz	-40 dB	4.5 dBi	able to determine
[22]	FR4	50×40	2 GHz-5 GHz	-35 dB	4.2 dBi	able to determine
Current work	FR4	18×21	6 GHz-14 GHz	-61 dB	5.8 dBi	able to determine

So, to cmpare with the existing literature, our current antenna has suitable outcomes for applying breast cancer detection. Actually, the MIT provides the fastest imaging inversion times [2, 4]. To reconstruct the image, several antennas are distributed around the breast phantom. A low-power microwave signal is transmitted from each antenna, and the system

registers and processes all the picked-up reflections [2]. The next step is to acquire the electromagnetic signals reflected from the breast for all combinations of all antennas. The process is repeated for different antenna heights. The medical doctor can view the reconstructed image after the signal acquisition. The algorithm computes the image for the whole volume, which can then be sliced into cuts for precise examination. The Microwave Radar-based Imaging Toolbox (MERIT) has been used to reconstruct an image from the backscattered signals [44]. The breast phantom is subjected to external electromagnetic radiation then some portion of the energy associated with electromagnetic radiation is absorbed by the phantom [45]. The amount of energy phantom absorbed is known as the SAR. This energy is responsible for raising the temperature of different phantom parts according to their dielectric properties. Usually, the effective treatment area in which the temperature rises 7 to 10 degrees is considered tumor necrosis [45]. However, there are some complexities to generalized applications of MIT. First, the experimental breast phantom is static, while real breast is dynamic. Second, designing an artificial breast phantom like the natural breast is challenging. There is some discrepancy in the dielectric properties of each layer of the artificial phantom to the real breast. Third, the time for the computation of relevant data is significantly longer than other processes, even a powerful computer is required to complete the simulation. Recently, different magnetic nanoparticles have been considered along with the microwave imaging process to determine the status of the breast tumor. Microwave Induced Thermoacoustic Imaging (MITI) is a modern imaging method in which electromagnetic microwave radiation is directly applied to the biological tissue to change the temperature of a specific portion of the tissue and for the generation of

thermal waves by expanding and contracting a particular medium of tissue [46-50]. Finally, the specific tissue medium's expansion and contraction produce acoustic sound waves. Several ultrasound transducers have detected these acoustic sound waves, utilized them to construct an image of a specific tissue part [47]. This method, which is a non-ionizing and non-conducting method, is simple, safe, and suitable for application in medical science, viz., early detection of different cancers as well as to diagnosis them, brain imaging, fetus during pregnancy, and cardiovascular imaging, etc. In MITI, microwave pulses are applied to a particular part of the tissue and the light-matter interaction produces different physical phenomena, viz., scattering, absorption, and reflection of the light, etc. But in this method, the absorption part is considered to observe the physical properties of the tissue [46-48]. So, when the microwave pulses are applied to the tissue, a local absorption of light is established, and the temperature of the associated regime increases, ultimately generating a sound wave. Several ultrasonic sensors are used to detect the acoustic sound waves. This sound wave has different physical properties, viz., amplitude, frequency, and phase, etc. The dielectric properties of the tissue with tumors and other abnormalities lead to a rigorous change in the amplitude, frequency, and phase of the sound wave [46-50]. So, the resulting images can provide detailed information about the tissue. This method has a unique high resolution and is easy to apply for differentiation of normal and abnormalities of tissue, and is very useful for the early detection of cancers.

Chapter 7
Conclusion

In this research work, we design amicrostrip patch antenna over the FR4 (lossy) substrate with an inverted T-type notch in the partial ground.Our current antenna is small size (30 mm × 30 mm × 1.6 mm)with a wideband operating frequency range of 6 to 14GHz. The maximum gain is reported at 5.8 dBi and the radiation pattern of the proposed antenna is almost omnidirectional in the operating frequency bandwidth. Compared with existing research, the proposed antenna has minimum return loss, high gain, is smaller in size, and is flexible to distribute around the breast phantom, etc.We have considered 8 antenna elements around the breast phantom. If we can consider more than 8 antennas around the breast phantom, then we can find more comprehensive information about the breast components. In future, the experimental set up will justify the simulated results associated with single antenna performance and antenna array around the breast phantom. Overall, we can employ this proposed antenna for early detection of a spherical breast tumor with a radius of 2, 5, 10, and 15mm in a deepseated position or arbitrary positions inside the breast phantom.

References

[1] S. S. Ahmed, J. F. Mahdi, and M. A. Kadhim, Design of ultra-wideband microwave antenna array for detection breast cancer tumors, *IOP Conference Series: Materials Science and Engineering*, 881, 012112 (2020).

[2] L. Wang, Early diagnosis of breast cancer. *Sensors*, 17, 1572 (2017).

[3] W. Alamro, B. C. Seet, L. Wang, and P. Parthiban, Early-stage lung tumor detection based on superwideband microwave reflectometry, *Electronics*, 12, 36 (2022).

[4] L. Wang, Microwave sensors for breast cancer detection, *Sensors*, 18, 655 (2018).

[5] M. Zeeshan, B. Salam, Q. S. B. Khalid, S. Alam, R. Sayani, Diagnostic accuracy of digital mammography in the detection of breast cancer, *Cureus*, 10, e2448 (2018).

[6] P. Jaglan, R. Dass, M. Duhan, Breast cancer detection techniques: issues and challenges, *J. Inst. Eng. India Ser. B,* 100, 379 (2019).

[7] R. Sood, A. F. Rositch, D. Shakoor, E. Ambinder, K. L. Pool, E. Pollack, D. J. Mollura, L. A. Mullen, S. C. Harvey, Ultrasound for breast cancer detection globally: a systematic review and meta-analysis, *J. Glob. Oncol.,* 2019, 01 (2019).

[8] S. K. Yang, N. Cho, W. K. Moon, The role of PET/CT for evaluating breast cancer. *Korean J. Radiol.,* 8, 429 (2007).

[9] N. Avril, C. A. Rosé, M. Schelling, J. Dose, W. Kuhn, S. Bense, W. Weber, S. Ziegler, H. Graeff, M. Schwaiger, Breast imaging with positron emission tomography and fluorine-18 fluorodeoxyglucose, *J. Clin. Oncol.,* 18, 3495 (2000).

[10] E. Desperito, L. Schwartz, K. M. Capaccione, B. T. Collins, S. Jamabawalikar, B. Peng, R. Patrizio, M. M. Salvatore, Chest CT for breast cancer diagnosis, *Life*, 12, 1699 (2022).

[11] S. Taha, W. R. Mohamed, M. A. Elhemely, A. O. El-Gendy, T. Mohamed, Tunable femtosecond laser suppresses the proliferation of breast cancer in vitro, *J. Photochem. Photobiol. B*, 240, 112665 (2023).

[12] G. C. Wishart, M. Campisi, M. Boswell, D. Chapman, V. Shackleton, S. Iddles, A. Hallett, P. D. Britton, The accuracy of digital infrared imaging for breast cancer detection in women undergoing breast biopsy, *Eur. J. Surg. Oncol. EJSO*, 36, 535 (2010).

[13] M. Mahmud, M. Islam, N. Misran, A. Almutairi, M. Cho, Ultra-Wideband (UWB) antenna sensor based microwave breast imaging: a review, *Sensors*, 18, 2951 (2018).

[14] A. M. Qashlan, R. W. Aldhaheri, K. H. Alharbi, A modified compact flexible vivaldi antenna array design for microwave breast cancer detection, *Appl. Sci.*, 12, 4908 (2022).

[15] L. Wang, Multi-Frequency holographic microwave imaging for breast lesion detection, *IEEE Access*, 07, 83984 (2019).

[16] C. A. Balanis, Antenna theory: Analysis and design (Fourth edition). Hoboken, New Jersey: Wiley (2016).

[17] D. M. Pozar, Microwave engineering (Fourth edition). Hoboken, New Jersey: Wiley (2012).

[18] R. Caliskan, S. S. Gültekin, D. Uzer, and Ö. Dündar, A microstrip patch antenna design for breast cancer detection, *Procedia-Social and Behavioral Sciences*, 195, 2905 (2015).

[19] V. Selvaraj, D. Baskaran, P. H. Rao, P. Srinivasan, and R. Krishnan, Breast tissue tumor analysis using wideband antenna and microwave scattering, *IETE Journal of Research*, 67, 49 (2021).

[20] M. Elsaadi, H. Muhmed, M. A. Alraheem, H. Miftah, and O. Salah, Square patch antenna for breast cancer diagnosis at 2.45GHz, *Circuits and Systems, 10,* 45 (2019).

[21] A. H. Rambe, M. Jusoh, S. S. Al-Bawri, and M. A. Abdelghany, Wearable UWB antenna-based bending and wet performances for breast cancer detection, *Computers, Materials Continua, 73,* 5575 (2022).

[22] A. Syed, N. Sobahi, M. Sheikh, R. Mittra, and H. Rmili, Modified 16-quasi log periodic antenna array for microwave imaging of breast cancer detection, *Applied Sciences, 12,* 147 (2021).

[23] Md. S. Islam, S. M. Kayser Azam, A. K. M. Zakir Hossain, M. I. Ibrahimy, and S. M. A. Motakabber, A low-profile flexible planar monopole antenna for biomedical applications, *Engineering Science and Technology, an International Journal, 35,* 101112 (2022).

[24] M. Elsaadi, H. Muhmed, M. A. Alraheem, H. Miftah, and O. Salah, Square patch antenna for beast cancer diagnosis at 2.45GHz, *Circuits and Systems, 10,* 45 (2019).

[25] A. AlOmairi and D. C. Atilla, Ultra-wide-band microstrip patch antenna design for breast cancer detection. *Electrica, 22,* 41 (2021).

[26] M. N. Rahman, M. T. Islam, M. Z. Mahmud, and M. Samsuzzaman, Compact microstrip patch antenna proclaiming super wideband characteristics, *Microwave and Optical Technology Letters, 59,* 2563 (2017).

[27] R. J. Chitra and V. Nagarajan, Design and development of koch fractal antenna, *2016 International Conference on Communication and Signal Processing (ICCSP),* 2294 (2016).

[28] V. Waladi, N. Mohammadi, Y. Zehforoosh, A. Habashi, and J. Nourinia, A novel modified startriangular fractal (MSTF) monopole antenna for super-wideband applications. *IEEE Antennas and Wireless Propagation Letters, 12,* 651 (2013).

[29] S. Singhal, Octagonal Sierpinski band-notched super-wideband antenna with defected ground structure and symmetrical feeding, *Journal of Computational Electronics, 17,* 1071 (2018).

[30] S. Singhal, Asymmetrically fed octagonal Sierpinski band-notched super-wideband antenna. *Journal of Computational Electronics, 16,* 210 (2017).

[31] T. Tewary, S. Maity, S. Mukherjee, A. Roy, P. P. Sarkar, et al., High gain miniaturized super-wideband microstrip patch antenna, *International Journal of Communication Systems, 35,* (2022).

[32] S. S. Bhatia, A. Sahni, and S. B. Rana, A novel design of compact monopole antenna with defected ground plane for wideband applications, *Progress In Electromagnetics Research M, 70,* 21 (2018).

[33] A. Guruva Reddy, M. Madhavi, and P. Rakesh Kumar, Compact slotted multiband patch antenna with defected ground structure for wireless communication, *Journal of Physics: Conference Series, 1706,* 012150 (2020).

[34] P. Merlin Teresa and G. Umamaheswari, Compact slotted microstrip antenna for 5G applications operating at 28 GHz, *IETE Journal of Research, 68,* 3778 (2022).

[35] A. Moradikordalivand and T. A. Rahman, Broadband modified rectangular microstrip patch antenna using stepped cut at four corner method, *Progress In Electromagnetics Research, 137,* 599 (2013).

[36] R. Przesmycki, M. Bugaj, and L. Nowosielski, Broadband microstrip antenna for 5G wireless systems operating at 28GHz, *Electronics, 10,* 01 (2020).

[37] Md. S. Islam, M. I. Ibrahimy, S. M. A. Motakabber, and A. K. M. Z. Hossain, A rectangular inset-fed patch antenna with defected ground structure for ISMband, *2018 7th International Conference on Computer and Communication Engineering (ICCCE),* 104 (2018).

[38] S. Shrestha, S. R. Lee, and D. Y. Choi, A new fractal-based miniaturized dual band patch antenna for RF energy harvesting, *International Journal of Antennas and Propagation, 2014, 0*1 (2014).

[39] E.A. Aydın and S. M. K. Kele, Breast cancer detection using K-nearest neighbors dataminingmethod obtained from the bow-tie antenna dataset, *International Journal of RF and Microwave Computer-Aided Engineering, 27,* e21098 (2017).

[40] M. Lazebnik, L. McCartney, D. Popovic, C. B. Watkins, M. J. Lindstrom, et al., A large-scale study of the ultrawideband microwave dielectric properties of normal breast tissue obtained from reduction surgeries, *Physics in Medicine and Biology, 52(10),* 2637 (2007).

[41] M. Lazebnik, D. Popovic, L. McCartney, C. B. Watkins, M. J. Lindstrom, et al., A largescale study of the ultrawideband microwave dielectric properties of normal, benign, and malignant breast tissues obtained from cancer surgeries *Physics in Medicine and Biology, 52,* 6093 (2007).

[42] Y. Cheng and M. Fu, Dielectric properties for non-invasive detection of normal, benign, andmalignant breast tissues usingmicrowave theories: Microwave properties of breast tissues, *Thoracic Cancer, 09,* 459 (2018).

[43] F. E. Zerrad, M. Taouzari, E. M. Makroum, S. Ahmad, F. O. Alkurt, et al., Symmetrical and asymmetrical breast phantoms with 3D-printed anatomical structure for microwave imaging of breast cancer, *IEEE Access, 10,* 96896 (2022).

[44] D. O'Loughlin, M. A. Elahi, E. Porter, A. Shahzad, B. L. Oliveira, M. Glavin, E. Jones, M. O'Halloran, Open-source software for microwave radar-based image reconstruction, *In Proceedings of the 12th European Conference on Antennas and Propagation (EuCAP 2018), London, UK,* 9–13 April, 408 (2018).

[45] S. Lim, Y. J. Yoon, Wideband-Narrowband switchable tapered slot antenna for breast cancer diagnosis and treatment, *Appl. Sci.,* 11, 3606 (2021).

[46] M. Soltani, Rahpeima, F. M. Kashkooli, Breast cancer diagnosis with a microwave thermoacoustic imaging technique—a numerical approach, *Med. Biol. Eng. Comput.*, 57, 1497 (2019).

[47] Y. Cui, C. Yuan, Z. Ji, A Review of microwave-induced thermoacoustic imaging: excitation source, data acquisition system and biomedical applications, *J. Innov. Opt. Health Sci.,* 10, 1730007 (2017).

[48] R. Rahpeima, M. Soltani, F. M. Kashkooli, Numerical study of microwave induced thermoacoustic imaging for initial detection of cancer of breast on anatomically realistic breast phantom, *Comput. Methods Programs Biomed.,* 196, 105606 (2020).

[49] A. Yan, L. Lin, C. Liu, J. Shi, S. Na, L. V. Wang, Microwave-induced thermoacoustic tomography through an adult human skull, *Med. Phys.,* 46, 1793 (2019).

[50] B. Wang, Y. Sun, Z. Wang, X. Wang, Three-Dimensional microwave-induced thermoacoustic imaging based on compressive sensing using an analytically constructed dictionary, *IEEE Trans. Microw. Theory Tech.,* 68, 377 (2020).